

## AUTHOR QUERY FORM

	Journal: J. Chem. Phys.  Article Number: JCP19-AR-05179	Please provide your responses and any corrections by annotating this PDF and uploading it to AIP's eProof website as detailed in the Welcome email.
---	---	---

Dear Author,

Below are the queries associated with your article. Please answer all of these queries before sending the proof back to AIP.

**Article checklist:** In order to ensure greater accuracy, please check the following and make all necessary corrections before returning your proof.

1. Is the title of your article accurate and spelled correctly?
2. Please check affiliations including spelling, completeness, and correct linking to authors.
3. Did you remember to include acknowledgment of funding, if required, and is it accurate?

Location in article	Query/Remark: click on the Q link to navigate to the appropriate spot in the proof. There, insert your comments as a PDF annotation.
<a href="#">Q1</a>	Please check that the author names are in the proper order and spelled correctly. Also, please ensure that each author's given and surnames have been correctly identified (given names are highlighted in red and surnames appear in blue).
<a href="#">Q2</a>	Figure 2 was not cited in the text. We have inserted a citation in the sentence beginning "Diffusion on the 1-D . . ." Please check and reposition if necessary.
<a href="#">Q3</a>	Figures 5 and 6 were not cited in the text. We have inserted a citation in the sentence beginning "The K12M mutant of . . ." Please check and reposition if necessary.
<a href="#">Q4</a>	Please reword the sentence beginning with "We have illustrated these problems . . ." so that your meaning will be clear to the reader.
<a href="#">Q5</a>	References (2 and 41), (18 and 23), (20 and 46), (21 and 28), and (42 and 48) contain identical information. Please check and provide the correct reference or delete the duplicate reference. If the duplicate is deleted, renumber the reference list as needed and update all citations in the text.
<a href="#">Q6</a>	Please provide publisher's name in Ref. 5.
<a href="#">Q7</a>	Please confirm the change in journal title in Ref. 8.
<a href="#">Q8</a>	If preprint Ref. 12 has subsequently been published elsewhere, please provide updated reference information (journal title, volume number, and page number).
<a href="#">Q9</a>	Please confirm the volume number and page number in Ref. 16, as we have inserted the required information.
<a href="#">Q10</a>	We were unable to locate a digital object identifier (doi) for Ref. 17. Please verify and correct author names and journal details (journal title, volume number, page number, and year) as needed and provide the doi. If a doi is not available, no other information is needed from you. For additional information on doi's, please select this link: <a href="http://www.doi.org/">http://www.doi.org/</a> .
<a href="#">Q11</a>	Please confirm the change in page number in Ref. 36.

*Continued on next page.*

*Continued from previous page.*

Please confirm ORCIDs are accurate. If you wish to add an ORCID for any author that does not have one, you may do so now. For more information on ORCID, see <https://orcid.org/>.

Hongbin Wan –

Vincent A. Voelz – 0000-0002-1054-2124

Please check and confirm the Funder(s) and Grant Reference Number(s) provided with your submission:

National Institute of General Medical Sciences, Award/Contract Number 1R01GM123296

Division of Computer and Network Systems, Award/Contract Number CNS-09-58854

NIH Office of the Director, Award/Contract Number S10-OD020095

Please add any additional funding sources not stated above.

Thank you for your assistance.

# 1 Adaptive Markov state model estimation 2 using short reseeding trajectories

3 Cite as: J. Chem. Phys. 152, 000000 (2020); doi: 10.1063/1.5142457

4 Submitted: 13 December 2019 • Accepted: 18 December 2019 •

5 Published Online: XX XX XXXX



6 **Hongbin Wan** and **Vincent A. Voelz<sup>a)</sup>**

## 7 AFFILIATIONS

8 Department of Chemistry, Temple University, Philadelphia, Pennsylvania 19122, USA

9 <sup>a)</sup>Electronic mail: [voelz@temple.edu](mailto:voelz@temple.edu)

## 11 ABSTRACT

12 In the last decade, advances in molecular dynamics (MD) and Markov State Model (MSM) methodologies have made possible accurate and  
13 efficient estimation of kinetic rates and reactive pathways for complex biomolecular dynamics occurring on slow time scales. A promising  
14 approach to enhanced sampling of MSMs is to use the so-called “adaptive” methods, in which new MD trajectories are “seeded” preferentially  
15 from previously identified states. Here, we investigate the performance of various MSM estimators applied to reseeding trajectory data, for  
16 both a simple 1D free energy landscape and mini-protein folding MSMs of WW domain and NTL9(1–39). Our results reveal the practical  
17 challenges of reseeding simulations and suggest a simple way to reweight seeding trajectory data to better estimate both thermodynamic and  
18 kinetic quantities.

19 Published under license by AIP Publishing. <https://doi.org/10.1063/1.5142457>

## 21 I. INTRODUCTION

22 In the last decade, Markov State Model (MSM) methodologies  
23 have made possible accurate and efficient estimation of kinetic rates  
24 and reactive pathways for slow and complex biomolecular dynamics.<sup>1–5</sup> One of the key advantages touted by MSM methods is the  
25 ability to use large ensembles of short-time scale trajectories for sam-  
26 pling events that occur on slow time scales. The main idea is that  
27 sufficient sampling using many short trajectories can circumvent the  
28 need to sample long trajectories.

29 With this in mind, many “adaptive” methods have been  
30 developed for the purpose of accelerating sampling of MSMs.  
31 The simplest of these can be called *adaptive seeding*, where one  
32 or more new rounds of unbiased simulations are performed by  
33 “seeding” swarms of trajectories throughout the landscape.<sup>6</sup> The  
34 choice of seeds is based on some initial approximation of the  
35 free energy landscape, possibly from nonequilibrium or enhanced-  
36 sampling methods. Adaptive seeding can be performed by first  
37 identifying a set of metastable states and then initiating sim-  
38 ulations from each state. If the seeding trajectories provide suffi-  
39 cient connectivity and statistical sampling of transition rates, an  
40 MSM can be constructed to accurately estimate both kinetics and  
41 thermodynamics.

42 Similarly, the so-called *adaptive sampling* algorithms have been  
43 developed for MSMs in which successive rounds of targeted seeding  
44 simulations are performed, updating the MSM after each round.<sup>7,8</sup>  
45 A simple adaptive sampling strategy is to start successive rounds  
46 of simulations from undersampled states, for instance, from the  
47 state with the least number of transition counts.<sup>9</sup> A more sophis-  
48 ticated approach is the FAST algorithm, which is designed to dis-  
49 cover states and reactive pathways of interest by choosing new  
50 states based on an objective function that balances undersampling  
51 with a reward for sampling desired structural observables.<sup>10,11</sup> Other  
52 algorithms include REAP, which efficiently explores folding land-  
53 scapes by using reinforcement learning to choose new states,<sup>12</sup> and  
54 surprisal-based sampling,<sup>7</sup> which chooses new states that will min-  
55 imize the uncertainty of the relative entropy between two or more  
56 MSMs.

57 A key problem with adaptive sampling of MSMs arises because  
58 we are often interested in *equilibrium* properties, while trajectory  
59 seeding is decidedly *nonequilibrium*. This may seem like a subtle  
60 point, because the dynamical trajectories themselves are unbiased,  
61 but of course, the ensemble of starting points for each trajectory are  
62 almost always *statistically* biased; i.e., the seeds are not drawn from  
63 the true equilibrium distribution. This can be problematic because  
64 most MSMs are constructed from transition rate estimators that

enforce detailed balance and assume trajectory data are obtained at equilibrium. The distribution of sampled transitions, however, will only reflect equilibrium conditions in the limit of long trajectory length.

One way around this problem is to focus mostly on the kinetic information obtained by adaptive sampling. A recent study of the ability of FAST to accurately describe reactive pathways concluded that the most reliable MSM estimator to use with adaptive sampling data is a row-normalized transition count matrix.<sup>11</sup> Indeed, weighted-ensemble path sampling algorithms focus mainly on sampling the kinetics of reactive pathways, information which can be used to recover global thermodynamic properties.<sup>13–17</sup> A major disadvantage of this approach is that it ignores potentially valuable equilibrium information. As shown by Trendelkamp-Schroer and Noé,<sup>18</sup> detailed balance is a powerful constraint to infer rare-event transition rates from equilibrium populations. Specifically, when faced with limited sampling, dedicating half of one's simulation samples toward enhanced thermodynamic sampling (e.g., umbrella sampling) can result in a significant reduction in the uncertainty of estimated rates, simply because the improved estimates of equilibrium state populations inform the rate estimates through detailed balance.

Another way around this problem, recently described by Nüske *et al.*, is to use an estimator based on observable operator model (OOM) theory, which utilizes information from transitions observed at lag times  $\tau$  and  $2\tau$  to obtain estimates unbiased by the initial distribution of seeding trajectories.<sup>19</sup> Although the OOM estimator is able to make better MSM estimates at shorter lag times, it requires the storage of transition count arrays that scale as the cube of the number states and dense-matrix singular-value decomposition, which can be impractical for MSMs with large numbers of states. Nüske *et al.* derived an expression quantifying the error incurred by nonequilibrium seeding, from which they conclude that such bias is difficult to remove without either increasing the lag time or improving the state discretization.

Here, we explore an alternative way to recover accurate MSM estimates from biased seeding trajectories, by reweighting sampled transition counts to better approximate counts that would be observed at equilibrium. Like the Trendelkamp-Schroer and Noé method,<sup>18</sup> this requires some initial estimate of state populations, perhaps obtained from the previous rounds of adaptive sampling.

We are particularly interested in examining how the performance of this reweighting method compares with other estimators, in cases where it is impractical to generate long trajectories and instead one must rely on ensembles of short seeding trajectories. An example of a case like this is adaptive seeding of protein folding MSMs built from ultralong trajectories simulated on the Anton supercomputer.<sup>20</sup> Because such computers are not widely available, adaptive seeding using conventional computers may be one of the only practical ways to leverage MSMs to predict the effect of mutations, for example.

In this manuscript, we first perform adaptive seeding tests using 1D-potential energy models and compare how different estimators perform at accurately capturing kinetics and thermodynamics. We then perform similar tests for MSMs built from ultralong reversible folding trajectories of two mini-proteins, WW domain and NTL9(1–39). Our results, described below, suggest that reweighting

trajectory counts with estimates of equilibrium state populations can achieve a good balance of kinetic and thermodynamic estimation.

## A. Estimators

We explored the accuracy and efficiency of several different transition probability estimators using adaptive seeding trajectory data as input: (1) a maximum-likelihood estimator (MLE), (2) an MLE estimator where the exact equilibrium populations  $\pi_i$  of each state  $i$  are known *a priori*, (3) an MLE estimator where each input trajectory is weighted by an *a priori* estimate of the equilibrium population of its starting state, (4) row-normalized transition counts, and (5) an observable operator model (OOM) estimator.

### B. Maximum-likelihood estimator (MLE)

The MLE for a reversible MSM assumes that observed transition counts are independent and drawn from the equilibrium distribution so that reversibility (i.e., detailed balance) can be used as a constraint. The likelihood of observing a set of given transition counts,  $L = \prod_i \prod_j p_{ij}^{c_{ij}}$ , when maximized under the constraint that  $\pi_i p_{ij} = \pi_j p_{ji}$ , for all  $i, j$ , yields a self-consistent expression that can be iterated to find the equilibrium populations,<sup>3,21,22</sup>

$$\pi_i = \sum_j \frac{c_{ij} + c_{ji}}{\frac{N_j}{\pi_j} + \frac{N_i}{\pi_i}}, \quad (1)$$

where  $N_i = \sum_j c_{ij}$ . The transition probabilities  $p_{ij}$  are given by

$$p_{ij} = \frac{(c_{ij} + c_{ji})\pi_j}{N_j\pi_i + N_i\pi_j}. \quad (2)$$

### C. Maximum-likelihood estimator (MLE) with known populations $\pi_i$

Maximization of the likelihood function above, with the additional constraint of fixed populations  $\pi_i$ , yields a similar self-consistent equation that can be used to determine a set of Lagrange multipliers,<sup>23</sup>

$$\lambda_i = \sum_j \frac{(c_{ij} + c_{ji})\pi_j\lambda_i}{\lambda_j\pi_i + \lambda_i\pi_j}, \quad (3)$$

from which the transition probabilities  $p_{ij}$  can be obtained as

$$p_{ij} = \frac{(c_{ij} + c_{ji})\pi_j}{\lambda_j\pi_i + \lambda_i\pi_j}. \quad (4)$$

### D. Maximum-likelihood estimator (MLE) with population-weighted trajectory counts

For this estimator, first a modified count matrix  $c'_{ij}$  is calculated,

$$c'_{ij} = \sum_k w^{(k)} c_{ij}^{(k)}, \quad (5)$$

where transition counts  $c_{ji}^{(k)}$  from trajectory  $k$  are weighted in proportion to  $w^{(k)} = \pi^{(k)}$ , the estimated equilibrium population of the initial state of the trajectory. The idea behind this approach is to counteract the statistical bias from adaptive seeding by scaling the

166 observed transition counts proportional to their equilibrium fluxes.  
167 The modified counts are then used as input to the MLE.

### 168 E. Row-normalized counts

169 For this estimator, the transition probabilities are approxi-  
170 mated as

$$171 p_{ij} = \frac{c_{ij}}{\sum_j c_{ij}}. \quad (6)$$

172 This approach does not guarantee reversible transition probabilities,  
173 which only occurs in the limit of large numbers of reversible transi-  
174 tion counts. In practice, however, the largest eigenvectors of the  
175 transition probability matrix have very nearly real eigenvalues such  
176 that we can report relevant relaxation time scales and equilibrium  
177 populations.

### 178 F. Observable operator model (OOM) theory

179 For an introduction to OOMs and their use in estimating  
180 MSMs, see Refs. 19, 24, and 25. OOMs are closely related to Hidden  
181 Markov Models (HMMs) but have the advantage, like MSMs,  
182 that they can be learned directly from observable-projected tra-  
183 jectory data.<sup>25</sup> Unlike MSMs, they require the collection of both  
184 one-step transition count matrices and a complete set of two-step  
185 transition count matrices. With enough training data and sufficient  
186 model rank, OOMs can recapitulate exact relaxation time scales,  
187 uncontaminated by MSM state discretization error.<sup>19</sup>

188 We used the OOM estimator as described by Nüske *et al.*<sup>19</sup>  
189 and implemented in PyEMMA 2.3,<sup>26</sup> using the default method of  
190 choosing the OOM model rank by discarding singular values that  
191 contribute a bootstrap-estimated signal-to-noise ratio of less than  
192 10. The settings used to instantiate the model in PyEMMA are as  
193 follows:

```
194 OOMReweightedMSM(reversible=True,  
195 count_mode='sliding', sparse=False,  
196 connectivity='largest',  
197 rank_Ct='bootstrap_counts', tol_rank=10.0,  
198 score_method='VAMP2', score_k=10,  
199 mincount_connectivity='1/n').
```

200 The OOM estimator returns two estimates: (1) a so-called *cor-  
201 rected* MSM, which derives from using the unbiased OOM equilib-  
202 rium correlation matrices to construct a matrix of MSM transition  
203 probabilities, and (2) the *OOM time scales*, which (given sufficient  
204 training data) estimate the relaxation time scales uncontaminated  
205 by discretization error. Note that there is no corresponding MSM  
206 for the OOM time scales.

## 207 II. RESULTS

### 208 A. A simple example of adaptive seeding 209 estimation error

210 To illustrate some of the estimation errors that can arise with  
211 adaptive seeding, we first consider a simple model of 1D diffusion  
212 over a potential energy surface  $V(x)$ . The continuous time evolution  
213 of a population distribution  $p(x, t)$  is analytically described by the  
214 Fokker-Planck equation,

$$215 \frac{\partial}{\partial t} p(x, t) = D \frac{\partial^2}{\partial x^2} p(x, t) + \mu \frac{\partial}{\partial x} [p(x, t) \nabla V(x)], \quad (7)$$

where  $D$  is the diffusion constant and  $\mu = D/k_B T$  is the mobility.  
Here,  $x$  and  $t$  are unitless values with  $D$  set to unity and the energy  
function  $V(x)$  in units of  $k_B T$ .

Here, we consider a “flat-bottom” landscape, over a range  
 $x \in (0, 2)$  with periodic boundaries, described by

$$221 V(x) = \frac{e^{-b(|x-1|-0.5)}}{1 + e^{-b(|x-1|-0.5)}}, \quad (8)$$

where  $b = 100$ . The landscape is partitioned into two states:  $x$  is  
assigned to state 0 if  $x < 0.5$  or  $x \geq 1.5$  and to state 1 otherwise  
[Fig. 1(a)]. In the limit of  $b \rightarrow \infty$ , the free energy difference between  
the states is exactly  $1/k_B T$ , with an equilibrium constant of  $K = e \approx 2.718$ . When  $b = 100$ ,  $K \approx 2.643$ . This value of  $b$  was chosen to help  
the stability of numerical integration (performed at a resolution of  
 $\Delta x = 2.5 \times 10^{-3}$  and  $\Delta t = 5 \times 10^{-7}$ ).

To emulate adaptive seeding, we propagate the continuous  
dynamics starting from an initial distribution  $p(x, 0)$  centered on  
state  $i$  and compute the transition probabilities  $p_{ij}$  from state  $i$  to  $j$   
from the evolved density after some lag time  $\tau$  [Fig. 1(b)].

We first consider a seeding strategy where simulations are  
started from the center of each state, which we model by propagating  
density from an initial distributions  $p(x, 0) = \delta(x)$  to compute  $p_{00}$  and  
 $p_{01}$  as a function of  $\tau$  and from  $p(x, 0) = \delta(x-1)$  to compute  $p_{10}$  and  
 $p_{11}$  [Fig. 1(c)]. By  $t = 1$ , the population has reached equilibrium. By  
detailed balance, the estimated equilibrium constant is  $\hat{K} = p_{10}/p_{01}$ ,  
which systematically *underestimates* the true value [Fig. 1(d)]. This  
is because the initial distribution is nonequilibrium, in the direction  
of being too uniform. There are also errors in estimating the relaxa-  
tion time scales. The different estimators described above (MLE,  
MLE with known equilibrium populations  $\pi_i$ , population-weighted  
MLE, and row-normalized counts) were applied to estimate the  
implied time scale  $\tau_2$  [Fig. 1(e)]. For this simple two-state sys-  
tem, all estimates are very similar to the analytical two-state result  
 $\tau_2 = -\tau/\ln(1 - p_{10} - p_{01})$  (with the exception of MLE, which yields  $\tau_2$   
estimates that are about 9% larger when  $t = 0.1$ ), which approaches  
the true slowest relaxation time scale of the Fokker-Plank dynamics  
( $\tau_2 = 0.1013$ ) as the lag time increases. Until the population density  
becomes equilibrated, however, the computed value of  $\tau_2$  is *overesti-  
mated*. This is because at early times, outgoing population fluxes are  
underestimated.

We also consider a seeding strategy where simulations are  
started from randomly from inside each state, which we model by  
propagating density from initially uniform distributions across each  
state [Fig. 1(f)]. As before, we find that the equilibrium constant is  
underestimated, again, because the initial seeding is out of equilibrium  
[Fig. 1(g)]. The estimate is somewhat improved, however, by the  
“pre-equilibration” of each state. In this case, the implied time  
scale  $\tau_2$  is *underestimated* at early times [Fig. 1(h)]. This can be  
understood as arising from the *overestimation* of outgoing popula-  
tion fluxes, as not enough population has yet reached the ground  
state (state 0).

From these two scenarios, we can readily understand that the  
success of estimating both kinetics and thermodynamics from adap-  
tive seeding greatly depends on how well the initial seeding dis-  
tribution approximates the equilibrium distribution. Moreover, we  
can see that time scale estimates can be either underestimated or  
overestimated, depending on the initial seeding distribution. It is

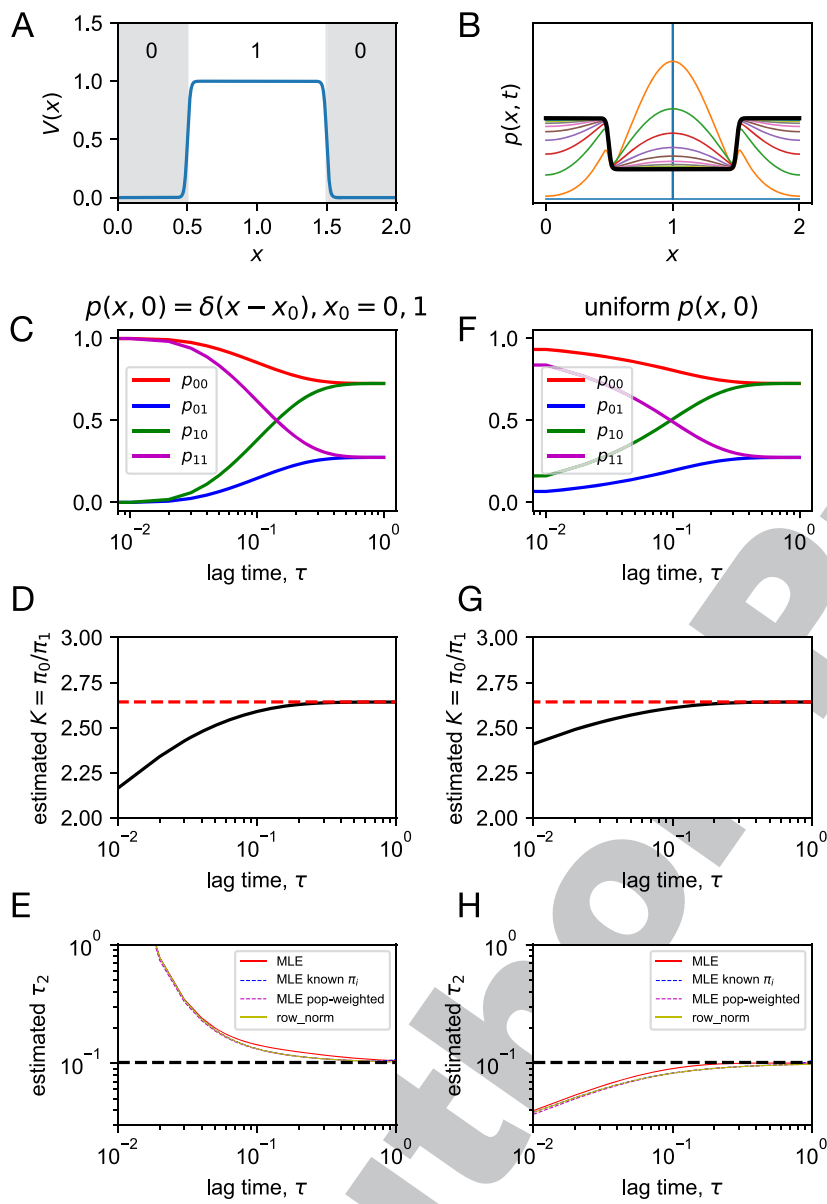


**FIG. 1.** Adaptive seeding in a simple two-state system. (a) The potential energy surface  $V(x)$ , annotated with state indices. (b) Propagation of an initial distribution  $p(x, 0) = \delta(x - 1)$  (blue), plotted at increments  $\Delta t = 0.1$ , up to  $t = 1$ . Starting from an initial distribution  $p(x, 0) = \delta(x - x_0)$  using  $x_0 = 0, 1$ , shown are estimated quantities as a function of lag time  $\tau$ : (c) transition probabilities  $p_{ij}$ , (d) equilibrium constant  $K = \pi_0/\pi_1$ , and (e) relaxation time scale  $\tau_2$ , as computed by various estimators. Starting from uniform distributions  $p(x, 0)$  over each state, shown are estimated quantities as a function of lag time  $\tau$ : (f) transition probabilities  $p_{ij}$ , (g) equilibrium constant  $K = \pi_0/\pi_1$ , and (h) relaxation time scale  $\tau_2$ , as computed by various estimators.

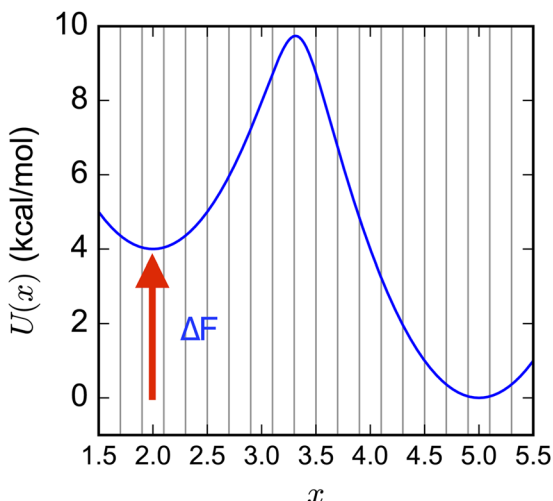
important to note that these errors arise primarily because of the nonequilibrium sampling rather than finite sampling error or discretization error.<sup>3</sup>

## B. Seeding of a 1-D potential energy surface

We next consider the following two-well potential energy surface, as used by Stelzl *et al.*<sup>27</sup>  $U(x) = -\frac{2k_B T}{0.596} \ln[e^{-2(x-2)^2/2} + e^{-2(x-5)^2}]$  for  $x \in [1.5, 5.5]$  and  $k_B T = 0.596$  kcal mol<sup>-1</sup>. The state space is uniformly divided into 20 states of width 0.2 to calculate discrete-state quantities. Diffusion on the 1-D landscape is approximated by a Markov Chain Monte Carlo (MCMC) procedure in which new

moves are translations randomly chosen from  $\delta \in [-0.05, +0.05]$  and accepted with probability  $\min(1, \exp(-\beta[U(x + \delta) - U(x)]))$ , i.e., the Metropolis criterion (Fig. 2).

As a standard against which to compare estimates from seeding trajectories, we used a set of very long trajectories to construct an optimal MSM model using the above state definitions. To estimate the “true” relaxation time scales of the optimal model, we generated long MCMC trajectories of  $10^9$  steps, sampling from a series of scaled potentials  $U^{(\lambda)}(x) = \lambda U(x)$  for  $\lambda \in [0.5, 0.6, 0.7, 0.8, 0.9, 1.0]$ . For each  $\lambda$  value, 20 trajectories were generated, with half of them starting from  $x = 2.0$  and the other half starting from  $x = 5.0$ , resulting in a total of 120 trajectories. The DTRAM estimator of Wu

314  
315  
316

**FIG. 2.** A 1-D two-state potential was used to test the performance of MSM estimators on seeding trajectory data. Vertical lines denote the 20 uniformly spaced discrete states.

*et al.*<sup>25</sup> was used to estimate the slowest relaxation time scale as  $9.66 (\pm 1.37) \times 10^6$  steps, using a lag time of 1000 steps.

We next generated adaptive seeding trajectory data for this system. We limited the lag time to  $\tau = 100$  steps and generated  $s$  trajectories ( $5 \leq s \leq 1000$ ) of length  $n\tau$  (for  $n = 10, 100, 1000$  by initiating MCMC dynamics from the center positions of all 20 bins. The resulting data consisted of  $20 \times s \times n$  transition counts between all states  $i$  and  $j$  in lag time  $\tau$ , stored in a  $20 \times 20$  count matrix of entries  $c_{ij}$ . From these counts, estimates of the transition probabilities,  $p_{ij}$ , were made.

Estimates of the slowest MSM implied time scales were computed as  $\tau_2 = -\tau/\ln \mu_2$ , where  $\mu_2$  is the largest nonstationary eigenvalue of the matrix of transition probabilities. Estimates of the free energy difference  $\Delta F$  between the two wells were computed as  $-k_B T \ln(\pi_L/(1 - \pi_L))$ , where  $\pi_L$  is the estimated total equilibrium population of MSM states with  $x < 3.3$ . To estimate uncertainties in  $\ln \tau_2$  and  $\Delta F$ , 20 bootstraps were constructed by sampling from the  $s$  trajectories with replacement.

Results for the five different estimators are shown in Fig. 3. In all cases, time scale estimates improve with larger numbers of seeding trajectories and greater numbers of steps in each trajectory. From these results, one can clearly see that MLE (red lines in

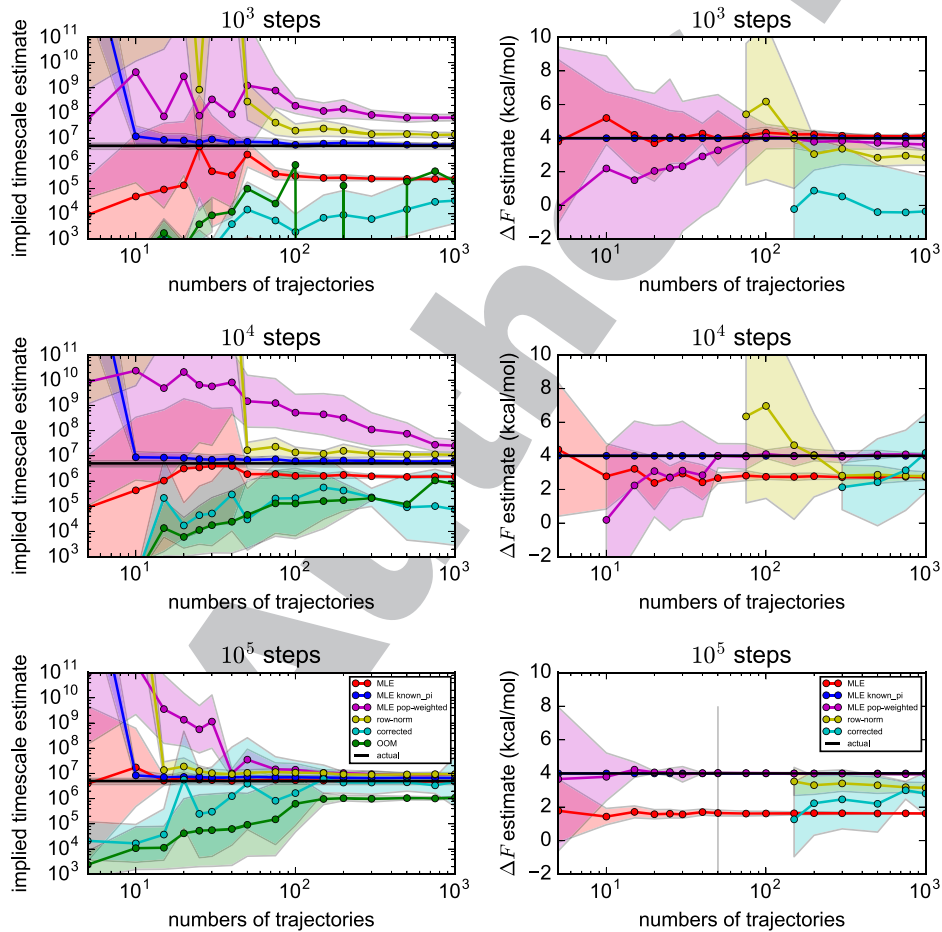


**FIG. 3.** Estimates of the slowest implied time scales (left) and two-well free energy differences (right), shown as a function of number of seeding trajectories of various lengths. Shown are results for (red) MLE, (blue) MLE with known equilibrium populations, (magenta) MLE with population-weighted trajectory counts, (yellow) row-normalized counts, (cyan) corrected MSMs, and (green) OOM time scales. Black horizontal lines denote the highly converged estimates from DTRAM. Shaded bounds represent uncertainties estimated from a bootstrap procedure.

317  
318  
319  
320  
321  
322  
323  
324  
325  
326  
327  
328  
329  
330  
331  
332  
333  
334  
335  
336  
337  
338339  
340  
341  
342  
343  
344  
345  
346  
347  
348  
349  
350  
351  
352  
353

Fig. 3), the default estimator in software packages like PyEMMA<sup>26</sup> and MSMBuilder,<sup>28</sup> consistently underestimates the implied time scale, although this artifact becomes less severe as more trajectory data is incorporated. At the same time, MLE estimates of equilibrium populations become systematically *worse* with more trajectory data. This is precisely because uniform seeding produces a biased, *nonequilibrium* distribution of sampled trajectories, but the MLE assumes that trajectory data are drawn from *equilibrium*. In contrast, the MLE with known equilibrium populations (blue lines in Fig. 3) accurately predicts implied time scales with much less trajectory data, underscoring the powerful constraint that detailed balance provides in determining rates. Of all the estimators, this method is the most accurate but relies on having very good estimates of equilibrium state populations *a priori*.

The row-normalized counts estimator (yellow lines in Fig. 3) estimates time scales well, provided that a sufficient number of observed transitions must be sampled to obtain proper estimates. This is necessary to achieve connectivity and to ensure that the transition matrix is at least approximately reversible. However, the free energy differences estimated by row-normalized counts are highly uncertain, and in the limit of large numbers of sufficiently long trajectories ( $10^5$  steps), estimates of free energies become systematically incorrect due to the statistical bias from seeding. In comparison, the MLE with population-weighted trajectory counts (magenta lines in Fig. 3) is able to make much more accurate estimates of free energies with less trajectory data. We note that while here we are reweighting the transition counts with the known populations, the results are similar if reasonable approximations of the state populations are used (data not shown). Compared with the row-normalized counts estimator, implied time scales are slower to converge with more trajectory data but are comparable when the seeding trajectories are sufficiently long ( $10^5$  steps). With sufficiently long trajectories ( $10^5$  steps), the MLE time scales are better estimated than either the row-normalized counts estimator or the population-weighted trajectory counts, but MLE is flawed because the free energies are so biased from the seeding. The population-weighting trajectory counts estimator avoids this artifact to give good estimates of free energies.

The “corrected” and OOM time scales from the OOM estimator consistently underestimate the slowest implied time scale for this test system, although these estimates improve with greater numbers and lengths of trajectories (cyan and green lines in Fig. 3). The OOM estimator is susceptible statistical noise, as evidenced by the average OOM model rank selected by the PyEMMA implementation, which increases from 2 to 10 as the numbers of trajectories are increased (Fig. 4). Like the row-normalized counts estimator, the OOM estimator gives poorly converged estimates of two-well free energy differences.

### C. Adaptive seeding of folding landscapes for WW domain and NTL9(1–39)

For studying protein folding, an adaptive seeding strategy may be useful for several reasons. For one, generating ensembles of short trajectories may simply be a practical necessity, due to the limited availability of special-purpose hardware to generate ultralong trajectories. Adaptive seeding may also be able to efficiently

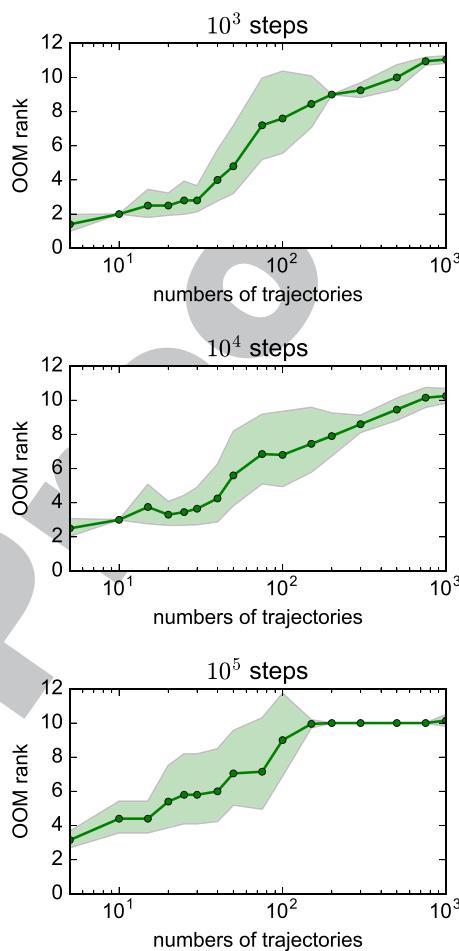


FIG. 4. The average OOM rank increases with the number of trajectories. Shaded bounds represent uncertainties estimated from a bootstrap procedure.

leverage an existing MSM (perhaps built from ultralong trajectory data) to predict perturbations to folding by mutations or to examine the effect of different simulation parameters like force field or temperature.

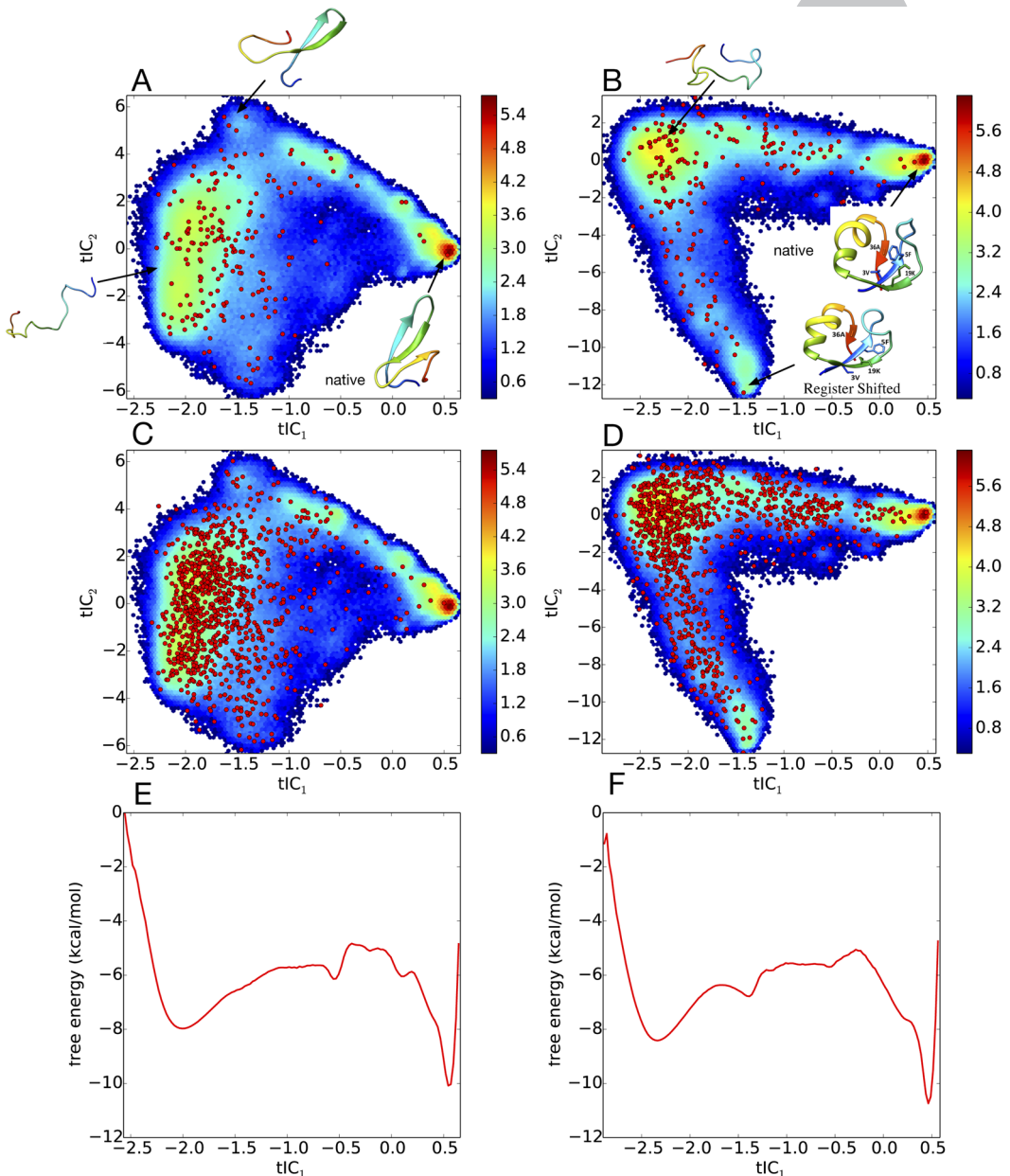
How can we best utilize adaptive seeding of MSMs built from ultralong trajectory data to make good estimates of both kinetics and thermodynamics? To address this question, here, we test the performance of various MSM estimators on the challenging task of estimating MSMs from adaptive seeding of protein folding landscapes. The folding landscapes come from MSMs built from ultralong reversible folding trajectories of fast-folding mini-proteins WW domain and NTL9(1–39).

WW domain is a 35-residue protein signaling domain with a three-stranded  $\beta$ -sheet structure that binds to proline-rich peptides. Its folding kinetics and thermodynamics have been studied extensively by time-resolved spectroscopy,<sup>30–34</sup> and its folding mechanism has been probed extensively using molecular simulation studies.<sup>35–37</sup> Moreover, an impressively large number of site-directed mutants of WW domain have been constructed to investigate folding

431 mechanism and discover fast-folding variants, including the Fip  
 432 mutant (Fip35) of human pin1 WW domain, for which mutations  
 433 in first hairpin loop region result in a fast folding time of  $\sim 13.3 \mu\text{s}$   
 434 at  $77.5^\circ\text{C}$ .<sup>41,42</sup> Further mutation of the second hairpin loop of Fip35  
 435 produced an even faster-folding variant, called GTT, in which the  
 436 native sequence Asn-Ala-Ser (NAS) was replaced with Gly-Thr-Thr  
 437 (GTT), resulting in a fast relaxation time  $\sim 4.3 \mu\text{s}$  at  $80^\circ\text{C}$ .<sup>43</sup>

NTL9(1–39) domain is a 39-residue truncation variant of the  
 442 N-terminal domain of ribosomal protein L9, whose folded state con-  
 443 sists of an  $\alpha$ -helix and a three-strand  $\beta$ -sheet. NTL9(1–39), which has  
 444 a folding relaxation time of  $\sim 1.5 \text{ ms}$  at  $25^\circ\text{C}$ ,<sup>44</sup> has been extensively  
 445 probed by both experimental and computational studies.<sup>40–44</sup> The  
 446 K12M mutant of NTL9(1–39) is a fast-folding variant with a folding  
 447 time scale of  $\sim 700 \mu\text{s}$  at  $25^\circ\text{C}$  (Figs. 5 and 6).<sup>40,45</sup>

448



438 FIG. 5. 200-state MSMs of (a) GTT WW domain and (b) K12M NTL9(1–39), built from ultralong folding trajectory data, are shown projected onto the two largest tICA  
 439 components. Red circles show the locations of the MSM microstates. The heat map shows a density plot of the raw trajectory data, with color bar values denoting the natural  
 440 logarithm of histogram counts. 1000-state MSMs are shown for (c) GTT WW domain and (d) K12M NTL9(1–39). (e) and (f) Corresponding 1-D free energy profiles along the  
 441 first tICA component, calculated from histogramming the trajectory data in bins of width 0.025.

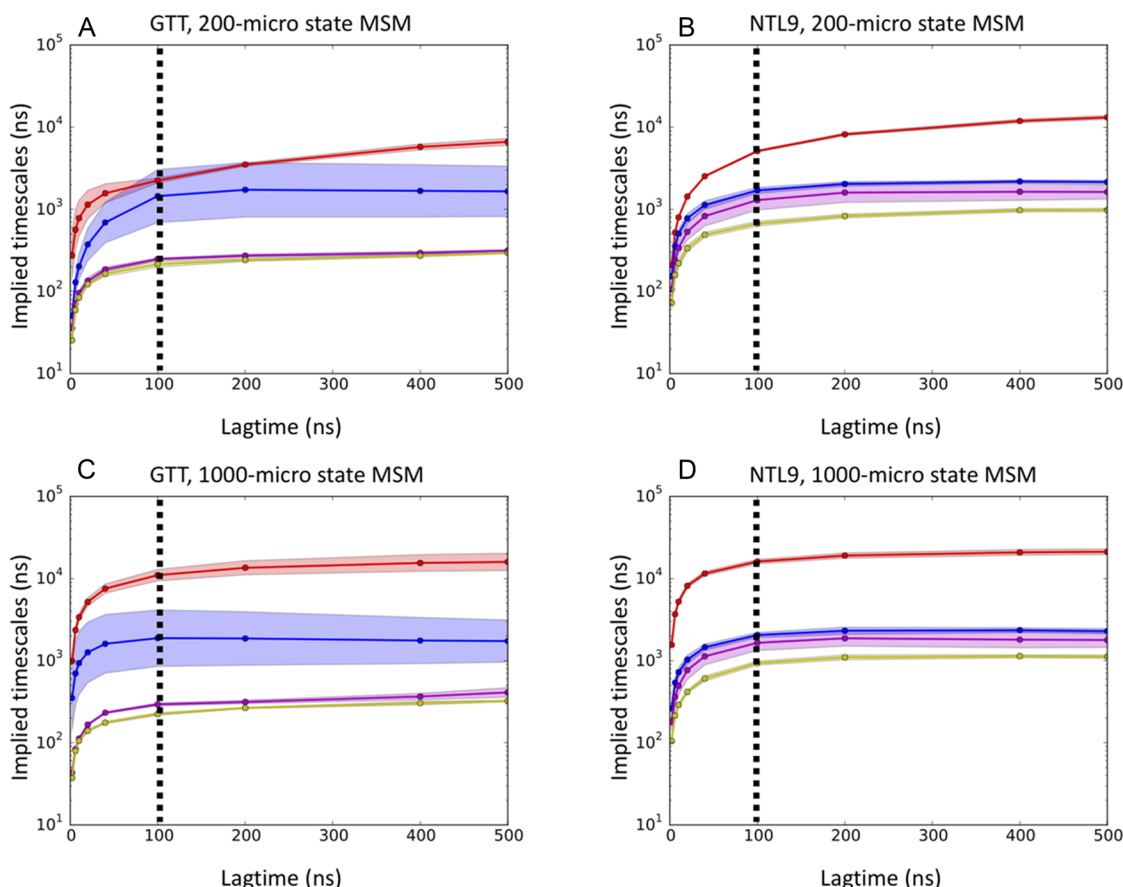


FIG. 6. Implied time scale plots for 200-state MSMs of (a) GTT WW domain and (b) K12M NTL9(1-39) and for 1000-state MSMs of (c) GTT WW domain and (d) K12M NTL9(1-39). Uncertainties (shaded areas) for GTT and NTL9 were estimated using 5-fold and 8-fold leave-one-out bootstraps, respectively. The dotted vertical line marks the lag time of 100 ns chosen to construct the MSMs.

449

450

451

#### 452 D. Markov state model construction

453 Molecular simulation trajectory data for GTT WW domain and  
454 K12M NTL9(1-39) were provided by Shaw *et al.*<sup>46</sup> Our first objec-  
455 tive was to construct high-quality reference MSMs from the available  
456 trajectory data, to be used as benchmarks against which we could  
457 compare adaptive seeding results.

458 Two independent ultralong trajectories of 651 and 486  $\mu$ s, per-  
459 formed at 360K using the CHARMM22\* force field, were used to  
460 construct MSMs of GTT WW domain, as previously described by  
461 Wan and Voelz.<sup>47</sup> The MSM was constructed by first projecting the  
462 trajectory data to all pairwise distances between C <sub>$\alpha$</sub>  and C <sub>$\beta$</sub>  atoms,  
463 performing dimensionality reduction via tICA (time-lagged inde-  
464 pendent component analysis),<sup>48,49</sup> and then clustering in this lower-  
465 dimensional space using the k-centers algorithm to define a set of  
466 metastable states. A 1000-state MSM for GTT WW domain was con-  
467 structed using a lag time of 100 ns. The generalized matrix Raleigh  
468 quotient (GMRQ) method<sup>50</sup> was used to choose the optimal number  
469 of states (1000) and the number of independent tICA components

470 (eight). The MSM gives an estimated folding relaxation time scale  
471 of 10.2  $\mu$ s, which is comparable with the folding time of 21  $\pm$  6  $\mu$ s  
472 estimated from the analysis of the trajectory data by Lindorff-Larsen  
473 *et al.*<sup>46</sup> It is also comparable with the 8  $\mu$ s time scale estimate from  
474 a three-state MSM model built using sliding constraint rate esti-  
475 mation by Beauchamp *et al.*<sup>51</sup> As described below, since seeding  
476 trajectory data for a 1000-state MSM were too expensive to analyze  
477 using the OOM estimator, we additionally built a 200-state model,  
478 using the same methods, which gives an estimated folding time scale  
479 of 2.3  $\mu$ s.

480 Four trajectories of the K12M mutant of NTL9(1-39), of  
481 lengths 1052  $\mu$ s, 990  $\mu$ s, 389  $\mu$ s, and 377  $\mu$ s, simulated at 355 K  
482 using the CHARMM22\* force field, were provided by Shaw *et al.*<sup>46</sup>  
483 Choosing a lag time of 200 ns, we constructed an MSM using the  
484 same methodology as GTT WW domain described above, resulting  
485 in a 1000-state model utilizing 6 tICA components, which gives a  
486 folding time scale estimate of ~18  $\mu$ s. Although this is a faster time  
487 scale than the experimentally measured value at 25 °C, it accurately  
488 reflects the time scale of folding events observed in the trajectory

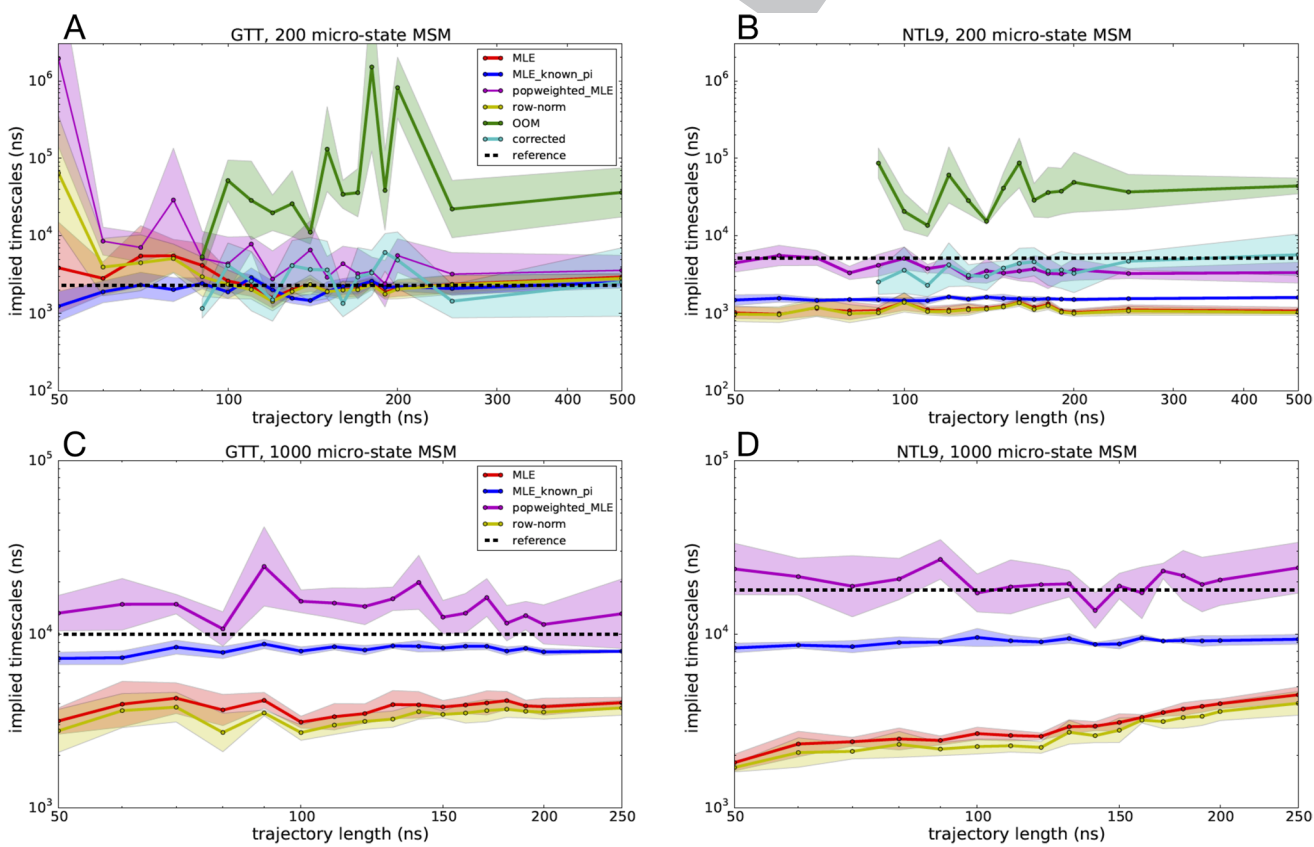
489 data (at 355 K) and is similar to folding time scales measured by T-  
490 jump 2-D IR spectroscopy at 80 °C (~26.4  $\mu$ s).<sup>44</sup> We also note that  
491 the previous analysis of the K12M NTL9(1–39) trajectory data has  
492 given similar time scale estimates. Analysis of the trajectory data  
493 by Lindorff-Larsen *et al.* yielded an estimate of ~29  $\mu$ s,<sup>44</sup> a three-  
494 state MSM model built using sliding constraint rate estimation by  
495 Beauchamp *et al.* gives an estimate of ~16  $\mu$ s,<sup>44</sup> and an MSM by  
496 Baiz *et al.* gives a time scale estimate of 18  $\mu$ s.<sup>44</sup> As we did for  
497 GTT WW domain, and using the same methods, we additionally  
498 built a 200-state MSM, which gives an estimated folding time scale  
499 of 5.2  $\mu$ s.

### E. Estimated folding rates and equilibrium populations from reseeding simulations

501 To emulate data sets that would be obtained by adaptive reseeding,  
502 we randomly sampled segments of the reference trajectory data  
503 that start from each metastable state. An advantage of emulating  
504 reseeding trajectory data in this way is the ability to recapitulate the  
505 original model in the limit of long trajectories. The full set of reference  
506 trajectory data (~1.1 ms) for GTT WW domain composed of  
507 12 reversible folding events, while the full set for K12M NTL9(1–39)  
508 (~2.8 ms) composed of 14 reversible folding events.

To test the performance of different estimators on reseeding trajectory data, we sampled either 5 or 10 seeding trajectories of various lengths from each MSM state. By design, the length of the reseeding trajectories was limited to 500 ns for the 200-state MSMs and to 250 ns for the 1000-state MSMs, because trajectories longer than this length result in data sets that exceed the total amount of reference trajectory data. For reseeding 1000-state MSMs with 10 trajectories, the trajectory lengths were limited to 100 ns for GTT and to 200 ns for NTL9 so as not to exceed the total amount of original trajectory data.

For each set of emulated reseeding trajectory data, MSMs were constructed using various estimators and compared with the reference MSM. Implied time scale estimates were computed using a lag time of 40 ns to facilitate the analysis of seeding trajectories as short as 50 ns. For the MLE estimator with population reweighting and the MLE estimator with known populations, we used the equilibrium populations estimated from the reference MSMs. In cases where the row-normalized counts estimator fails at large lag times due to the disconnection of states, a single pseudocount was added to the elements of the transition count matrix that are nonzero in the reference MSM.



509 FIG. 7. Slowest implied time scales predicted by various MSM estimators as a function of seeding trajectory length, where five independent trajectories were started from  
510 each microstate. Estimated slowest time scales are shown for 200-microstate MSMs of (a) GTT WW domain and (b) K12M NTL9(1–39) and for 1000-microstate MSMs of (c)  
511 GTT WW domain and (d) K12M NTL9(1–39). Uncertainties were computed using a bootstrap procedure.

### 1. Estimates of slowest implied time scales

We applied different estimators to the reseeding trajectory data generated for 200-state and 1000-state MSMs of GTT WW domain and K12M NTL9(1–39) and compared the predicted slowest implied time scales to the reference MSMs. Similar implied time scale estimates were obtained using five independent reseeding trajectories initiated from each state (Fig. 7) and ten independent reseeding trajectories (Fig. 8).

Across most of the estimators tested, implied time scale estimates are statistically well converged using trajectories of 100 ns or more. For the MLE-based estimators in particular (MLE, MLE with known populations, MLE with population reweighting), the estimates have small uncertainties and are not strongly sensitive to trajectory lengths tested. This suggests that while there is enough seeding data to combat statistical sampling error, there remain systematic errors in estimated time scales, mainly due to the estimation method used.

The MLE performs well for the 200-state MSMs of GTT but consistently underestimates the slowest implied time scale in all other MSMs. As seen with our tests above with the 1-D two-state potential, this error is likely due to using a detailed balance

constraint with statistically biased seeding trajectory data. The MLE with known populations is much more accurate at estimating the slowest implied time scale and with less uncertainty. For the NLT9 MSMs, however, the MLE with known populations systematically underestimates the slowest implied time scale, again suggesting that the biased seeding trajectory data have an influence despite the strong constraints enforced by the estimator. MLE with population reweighting has more uncertainty than the other MLE-based estimators but overall is arguably the most accurate estimator across all the MSM reseeding tests.

The OOM-based estimates of the slowest implied time scale (which could only be performed for the computationally tractable 200-state MSMs) required seeding trajectory data of least 90 ns, in order to have sufficient trajectory data to perform the bootstrapped signal-to-noise estimation, from which the OOM rank is selected. While the predicted OOM time scales overestimate the relaxation time scales of the 200-state MSMs of both GTT and NTL9 systems, the time scale estimates from the corrected MSMs more closely recapitulate the reference MSMs time scales, with accuracy comparable with the MLE with population reweighting, especially for seeding trajectories over 200 ns.

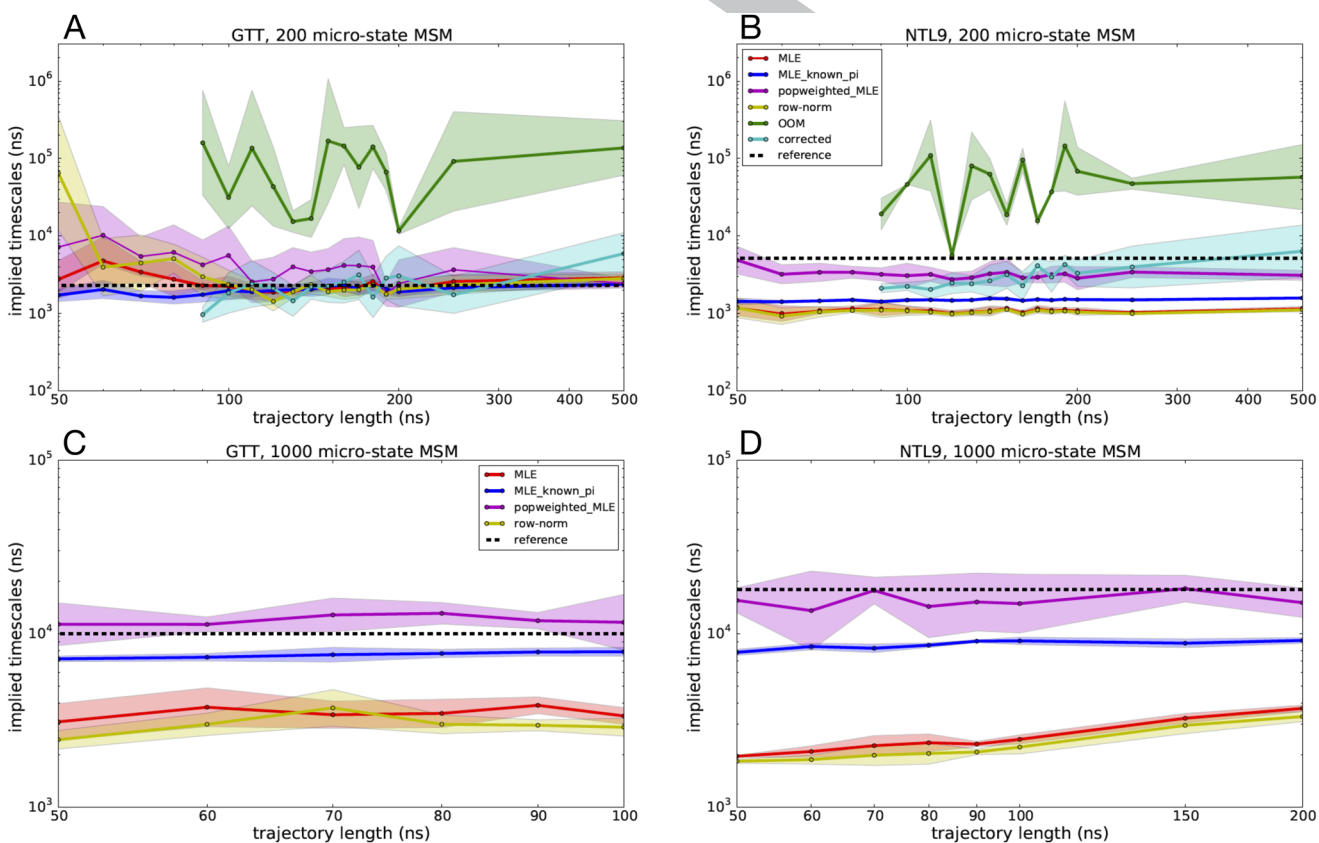


**FIG. 8.** Slowest implied time scales predicted by various MSM estimators as a function of seeding trajectory length, where ten independent trajectories were started from each microstate. Estimated slowest time scales are shown for 200-microstate MSMs of (a) GTT WW domain and (b) K12M NTL9(1–39) and for 1000-microstate MSMs of (c) GTT WW domain and (d) K12M NTL9(1–39). Trajectory lengths longer than 100 ns for GTT WW domain and 200 ns for K12M NTL9(1–39) result in trajectory data sets larger than the reference model and are not shown. Uncertainties were computed using a bootstrap procedure.

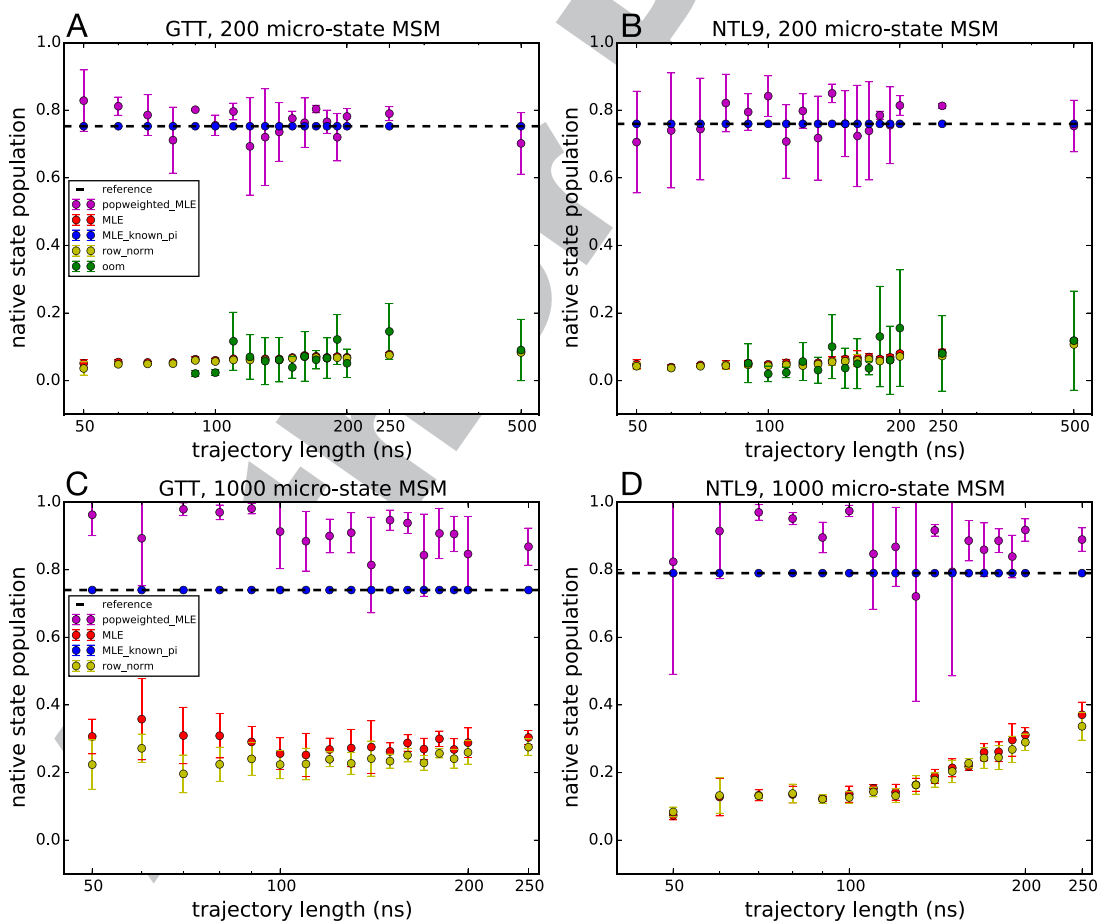
579      The row-normalized counts estimator yields slowest implied  
580      time scales estimates accelerated compared with the reference MSM,  
581      similar to the MLE results. This acceleration is greater than might be  
582      expected given our tests with the 1-D two-state potential and may in  
583      part be due to the necessity of adding pseudocounts to the transition  
584      count matrix to ensure connectivity.

## 585 **2. Estimates of native-state populations**

586      We applied different estimators to the reseeding trajectory  
587      data generated for 200-state and 1000-state MSMs of GTT WW  
588      domain and K12M NTL9(1–39) and compared the predicted  
589      native-state populations with the reference MSMs. The native-  
590      state population was calculated as the equilibrium population of  
591      the MSM state corresponding to the native conformation. Similar  
592      native-state populations were estimated using five independent  
593      reseeding trajectories initiated from each state (Fig. 9) and  
594      ten independent reseeding trajectories (Fig. 10). These estimates  
595      are compared with the native-state populations estimated from the

596      reference MSMs: 75.3% and 74.8% for the 200-state and 1000-  
597      state MSMs of GTT WW domain, respectively, and 75.9% and  
598      79.4% for the 200-state and 1000-state MSMs of K12M NTL9(1–39),  
599      respectively.

600      As we saw in our tests using a 1-D two-state potential, obtaining  
601      accurate estimates of the equilibrium populations from very short  
602      seeding trajectories is a challenging task. In those tests, we found  
603      that the most accurate estimates of native-state populations come  
604      from estimators that utilize some *a priori* knowledge of native-state  
605      populations. Here, the MLE with known populations recapitulates  
606      the native population exactly (by definition), while the MLE with  
607      population reweighting successfully captures the native-state popu-  
608      lation in a 200 microstate model of both GTT and NTL9 and slightly  
609      overestimates the native state population for the 1000-state MSMs.  
610      In contrast, the MLE, row-normalized counts, and OOM estima-  
611      tors all underestimate the folded populations. With the exception of  
612      some slight improvement that begins to occur as the seeding tra-  
613      jectory length increases, these underestimates are independent of  
614      the trajectory length, indicating that the nonequilibrium seeding is  
615      616      617



596      **FIG. 9.** Native state populations predicted by various MSM estimators as a function of seeding trajectory length. Estimated populations are shown for 200-microstate MSMs  
597      of (a) GTT WW domain and (b) K12M NTL9(1–39) and for 1000-microstate MSMs of (c) GTT WW domain and (d) K12M NTL9(1–39). Adaptive seeding data were generated  
598      using five independent trajectories from each microstate. Uncertainties were computed using a bootstrap procedure.

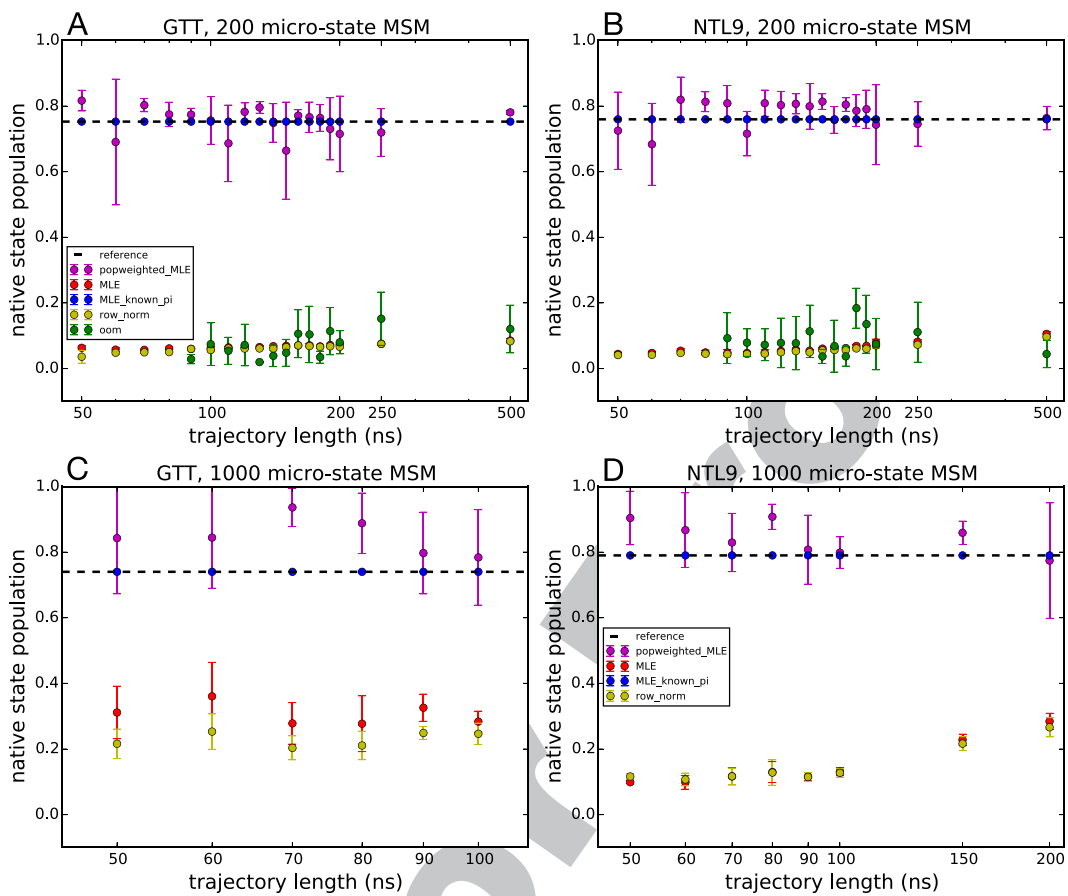


FIG. 10. Native state populations predicted by various MSM estimators as a function of seeding trajectory length. Estimated populations are shown for 200-microstate MSMs of (a) GTT WW domain and (b) K12M NTL9(1–39) and for 1000-microstate MSMs of (c) GTT WW domain and (d) K12M NTL9(1–39). Adaptive seeding data were generated using ten independent trajectories from each microstate. Trajectory lengths longer than 100 ns for GTT WW domain and 200 ns for K12M NTL9(1–39) result in trajectory data sets larger than the reference model and are not shown. Uncertainties were computed using a bootstrap procedure.

to blame. The native state populations are underestimated in these cases because there are many more MSM microstates belonging to the unfolded-state basin of the folding landscape.

### III. DISCUSSION

Markov state model approaches have enjoyed great success in the last decade due to their ability to integrate ensembles of short trajectories. In light of this success, the allure of adaptive sampling methods, which promises to leverage the focused sampling of short trajectories, is understandable. Recent studies have shown that a judiciously chosen adaptive sampling strategy can accelerate barrier crossing, state discovery, and pathway sampling.<sup>11,24</sup>

Our work in this manuscript underscores that a key problem with the practical use of adaptive sampling algorithms is the statistical bias introduced by focused sampling, which makes difficult the unbiased estimation of both kinetics and thermodynamics. We have illustrated these problems in simple 1D diffusion models and

in large-scale all-atom simulations of protein folding by testing the performance of various MSM estimators on adaptive seeding data generated these scenarios. In all cases, we find that estimators that incorporate some form of *a priori* knowledge about equilibrium populations are able to correct for sampling bias to some extent, resulting in accurate estimates of both slowest implied time scales and equilibrium free energies. Moreover, we have shown that an MLE estimator with population-weighted transition counts is a very simple way to counteract this bias and achieves reasonably accurate results.

As pointed out by others previously,<sup>18</sup> the success of such estimators is further demonstration of the importance of incorporating thermodynamic information into MSM estimates, given the powerful constraint that detailed balance provides. With this in mind, it is no surprise that new multiensemble MSM estimators like TRAM<sup>33</sup> and DHAMed<sup>27</sup> have been able to achieve more accurate results than previous estimators. Thus, while many existing adaptive sampling strategies focus sampling to refine estimated transition rates between states, we expect that improved adaptive sampling

estimators may come from similar “on-the-fly” focusing that seeks to refine thermodynamic estimates as well.

As adaptive sampling strategies and estimators continue to improve, we expect the more efficient use of ultralong simulation trajectories combined with ensembles of short trajectories for adaptive sampling, especially to probe the effects of protein mutations, or different binding partners for molecular recognition.

## ACKNOWLEDGMENTS

The authors thank the participants of Folding@home, without whom this work would not be possible. We thank D. E. Shaw Research for providing access to folding trajectory data. This research was supported in part by the National Science Foundation through major research instrumentation Grant No. CNS-09-58854 and the National Institutes of Health Grant No. 1R01GM123296 and NIH Research Resource Computer Cluster Grant No. S10-OD020095.

## REFERENCES

- 1 F. Noé, C. Schütte, E. Vanden-Eijnden, L. Reich, and T. R. Weikl, *Proc. Natl. Acad. Sci. U. S. A.* **106**, 19011 (2009).
- 2 V. A. Voelz, G. R. Bowman, K. Beauchamp, and V. S. Pande, *J. Am. Chem. Soc.* **132**, 1526 (2010).
- 3 J.-H. Prinz, H. Wu, M. Sarich, B. Keller, M. Senne, M. Held, J. D. Chodera, C. Schütte, and F. Noé, *J. Chem. Phys.* **134**, 174105 (2011).
- 4 J. D. Chodera and F. Noé, *Curr. Opin. Struct. Biol.* **25**, 135 (2014).
- 5 F. Noé, J. Chodera, G. Bowman, V. Pande, and F. Noé, *An Introduction to Markov State Models and Their Application to Long Timescale Molecular Simulation*, Advances in Experimental Medicine and Biology Vol. 797 (■, 2014).
- 6 X. Huang, G. R. Bowman, S. Bacallado, and V. S. Pande, *Proc. Natl. Acad. Sci. U. S. A.* **106**, 19765 (2009).
- 7 V. A. Voelz, B. Elman, A. M. Razavi, and G. Zhou, *J. Chem. Theory Comput.* **10**, 5716 (2014).
- 8 Z. Shamsi, A. S. Moffett, and D. Shukla, *Sci. Rep.* **7**, 12700 (2017).
- 9 S. Doerr and G. De Fabritiis, *J. Chem. Theory Comput.* **10**, 2064 (2014).
- 10 M. I. Zimmerman and G. R. Bowman, *J. Chem. Theory Comput.* **11**, 5747 (2015).
- 11 M. I. Zimmerman, J. R. Porter, X. Sun, R. R. Silva, and G. R. Bowman, *J. Chem. Theory Comput.* **14**, 5459 (2018).
- 12 Z. Shamsi, K. J. Cheng, and D. Shukla, preprint arXiv:1710.00495 (2017).
- 13 B. W. Zhang, D. Jasnow, and D. M. Zuckerman, *J. Chem. Phys.* **132**, 054107 (2010).
- 14 M. C. Zwier, J. L. Adelman, J. W. Kaus, A. J. Pratt, K. F. Wong, N. B. Rego, E. Suárez, S. Lettieri, D. W. Wang, M. Grabe, D. M. Zuckerman, and L. T. Chong, *J. Chem. Theory Comput.* **11**, 800 (2015).
- 15 A. Dickson and S. D. Lotz, *J. Phys. Chem. B* **120**, 5377 (2016).
- 16 S. D. Lotz and A. Dickson, *J. Am. Chem. Soc.* **140**, 618 (2018).
- 17 T. Dixon, S. D. Lotz, and A. Dickson, *J. Comput.-Aided Mol. Des.* **15**, 547 (2018).
- 18 B. Trendelkamp-Schroer and F. Noe, *Phys. Rev. X* **6**, 011009 (2016).
- 19 F. Nüske, H. Wu, J.-H. Prinz, C. Wehmeyer, C. Clementi, and F. Noé, *J. Chem. Phys.* **146**, 094104 (2017).
- 20 K. Lindorff-Larsen, S. Piana, R. O. Dror, and D. E. Shaw, *Science* **334**, 517 (2011).
- 21 H. Wu, A. S. J. S. Mey, E. Rosta, and F. Noé, *J. Chem. Phys.* **141**, 214106 (2014).
- 22 G. R. Bowman, K. A. Beauchamp, G. Boxer, and V. S. Pande, *J. Chem. Phys.* **131**, 124101 (2009).
- 23 B. Trendelkamp-Schroer and F. Noé, *Phys. Rev. X* **6**, 011009 (2016).
- 24 H. Jaeger, *Neural Comput.* **12**, 1371 (2000).
- 25 H. Wu, J.-H. Prinz, and F. Noé, *J. Chem. Phys.* **143**, 144101 (2015).
- 26 M. K. Scherer, B. Trendelkamp-Schroer, F. Paul, G. Perez-Hernandez, M. Hoffmann, N. Plattner, C. Wehmeyer, J.-H. Prinz, and F. Noé, *J. Chem. Theory Comput.* **11**, 5525 (2015).
- 27 L. S. Stelzl, A. Kells, E. Rosta, and G. Hummer, *J. Chem. Theory Comput.* **13**, 6328 (2017).
- 28 H. Wu, A. S. J. S. Mey, E. Rosta, and F. Noé, *J. Chem. Phys.* **141**, 214106 (2014).
- 29 M. P. Harrigan, M. M. Sultan, C. X. Hernández, B. E. Husic, P. Eastman, C. R. Schwantes, K. A. Beauchamp, R. T. McGibbon, and V. S. Pande, *Biophys. J.* **112**, 10 (2017).
- 30 H. Nguyen, M. Jäger, A. Moretto, M. Gruebele, and J. W. Kelly, *Proc. Natl. Acad. Sci. U. S. A.* **100**, 3948 (2003).
- 31 M. Jäger, Y. Zhang, J. Bieschke, H. Nguyen, M. Dendle, M. E. Bowman, J. P. Noel, M. Gruebele, and J. W. Kelly, *Proc. Natl. Acad. Sci. U. S. A.* **103**, 10648 (2006).
- 32 F. Liu and M. Gruebele, *Chem. Phys. Lett.* **461**, 1 (2008).
- 33 K. Dave, M. Jäger, H. Nguyen, J. W. Kelly, and M. Gruebele, *J. Mol. Biol.* **428**, 1617 (2016).
- 34 F. Liu, D. Du, A. A. Fuller, J. E. Davoren, P. Wipf, J. W. Kelly, and M. Gruebele, *Proc. Natl. Acad. Sci. U. S. A.* **105**, 2369 (2008).
- 35 Y. Gao, C. Zhang, X. Wang, and T. Zhu, *Chem. Phys. Lett.* **679**, 112 (2017).
- 36 R. B. Best, G. Hummer, and W. A. Eaton, *Proc. Natl. Acad. Sci. U. S. A.* **110**, 17874 (2013).
- 37 S. Piana, K. Sarkar, K. Lindorff-Larsen, M. Guo, M. Gruebele, and D. E. Shaw, *J. Mol. Biol.* **405**, 43 (2011).
- 38 H. Nguyen, M. Jäger, J. W. Kelly, and M. Gruebele, *J. Phys. Chem. B* **109**, 15182 (2005).
- 39 J.-C. Horng, V. Moroz, and D. P. Raleigh, *J. Mol. Biol.* **326**, 1261 (2003).
- 40 J.-H. Cho and D. P. Raleigh, *J. Mol. Biol.* **353**, 174 (2005).
- 41 V. A. Voelz, G. R. Bowman, K. Beauchamp, and V. S. Pande, *J. Am. Chem. Soc.* **132**, 1526 (2010).
- 42 C. R. Schwantes and V. S. Pande, *J. Chem. Theory Comput.* **9**, 2000 (2013).
- 43 J.-H. Cho, W. Meng, S. Sato, E. Y. Kim, H. Schindelin, and D. P. Raleigh, *Proc. Natl. Acad. Sci. U. S. A.* **111**, 12079 (2014).
- 44 C. R. Baiz, Y.-S. Lin, C. S. Peng, K. A. Beauchamp, V. A. Voelz, V. S. Pande, and A. Tokmakoff, *Biophys. J.* **106**, 1359 (2014).
- 45 J.-H. Cho, S. Sato, and D. P. Raleigh, *J. Mol. Biol.* **338**, 827 (2004).
- 46 K. Lindorff-Larsen, S. Piana, R. O. Dror, and D. E. Shaw, *Science* **334**, 517 (2011).
- 47 H. Wan, G. Zhou, and V. A. Voelz, *J. Chem. Theory Comput.* **12**, 5768 (2016).
- 48 C. R. Schwantes and V. S. Pande, *J. Chem. Theory Comput.* **9**, 2000 (2013).
- 49 G. Perez-Hernandez, F. Paul, T. Giorgino, G. De Fabritiis, and F. Noé, *J. Chem. Phys.* **139**, 015102 (2013).
- 50 R. T. McGibbon and V. S. Pande, *J. Chem. Phys.* **142**, 124105 (2015).
- 51 K. A. Beauchamp, R. McGibbon, Y.-S. Lin, and V. S. Pande, *Proc. Natl. Acad. Sci. U. S. A.* **109**, 17807 (2012).
- 52 E. Hruska, J. R. Abella, F. Nüske, L. E. Kavraki, and C. Clementi, *J. Chem. Phys.* **149**, 244119 (2018).
- 53 H. Wu, F. Paul, C. Wehmeyer, and F. Noé, *Proc. Natl. Acad. Sci. U. S. A.* **113**, E3221 (2016).